

A three-dimensional photometric model of a satellite in geostationary orbit

Jovan Skuljan

Defence Technology Agency, Auckland, New Zealand

ABSTRACT

A comprehensive three-dimensional photometric model was developed at the Defence Technology Agency (DTA) to study the light curves of satellites in geostationary orbit (GEO). The model treats a satellite as a collection of small flat facets, where each facet has its own light-reflection properties. A complete three-dimensional lighting geometry was considered, including the direct sunlight, moonlight and earthshine (the sunlight reflected from the Earth). The reflection of light was modelled based on the Ashikhmin-Shirley anisotropic bidirectional reflectance distribution function (BRDF), which ensures energy conservation, while allowing for both the diffuse and specular components of the reflection. Special attention was placed on the earthshine component of the lighting model, as this was found to be the predominant source of illumination at large solar phase angles. The illuminated part of the Earth was modelled as an extended source of light, while taking into account both the geographic and seasonal variations of the surface albedo across the globe. This was based on the data from the Global Ozone Monitoring Experiment (GOME), an instrument aboard the European Space Agency's (ESA) Second European Remote Sensing Satellite (ERS-2).

The software implementation of the model was written in Delphi. The application has a built-in module for the orbital positions of the Sun, Earth and Moon, based on the Jet Propulsion Laboratory's (JPL) solar system ephemeris DE441 (with an option for a different ephemeris file to be selected instead). All coordinate transformations are performed using the International Astronomical Union's (IAU) Standards of Fundamental Astronomy (SOFA) library, in combination with the current values for the Earth orientation parameters (EOP). In addition, the built-in SGP4 propagator converts the TLE parameters into a state vector, to complete the viewing geometry. This allows the program to generate the apparent magnitudes for any observer over the specified time interval.

The DTA photometric model was tested using a number of observations of GEO satellites over the Pacific, collected from the DTA Space Domain Awareness (SDA) Observatory at Whangaparaoa Peninsula near Auckland, New Zealand. An 11-inch (279-mm) Celestron Edge HD Cassegrain telescope on a Paramount MEII robotic mount was used, equipped with a Finger Lakes Instrumentation (FLI) ML-11002 CCD camera. All observations were reduced using StarView, an SDA image analysis tool developed at DTA for astrometric, photometric and polarimetric measurements of satellite observations. The second data release (DR-2) of the ESA's GAIA catalogue, limited down to magnitude 16, was used for data calibration. A typical photometric calibration based on the GAIA G-band produced an RMS error of about 0.1 magnitudes, mainly caused by stellar colours. At the same time, the random measurement errors in the aperture photometry were about 0.02, over a wide range of apparent magnitudes.

A number of light curves of selected objects in the GEO belt were collected and compared with the model predictions, for a broad range of input parameters, such as the satellite's overall shape and size, as well as the reflectivity properties of the individual facets. It was demonstrated that inexpensive small-aperture optical equipment can be successfully used to examine the photometric properties of satellites in GEO regime and collect important information for space domain awareness.

1. INTRODUCTION

The Defence Technology Agency (DTA) of the New Zealand Defence Force (NZDF) operates a small Space Domain Awareness (SDA) observatory located at Whangaparaoa Peninsula near Auckland [1,2]. Over the past several years, the observatory has been used to collect astrometric, photometric and polarimetric measurements of satellites both in low Earth orbit (LEO) and in geostationary (GEO) regime over the South Pacific Ocean. The observatory is equipped with two 28-cm telescopes: a Celestron Edge HD Cassegrain, for narrow-field imaging (approximately one degree diagonal field of view), and a Rowe-Ackermann Schmidt Astrograph (RASA), for wider fields of about four degrees diagonal, both using a Finger Lakes Instrumentation (FLI) ML-11002 CCD camera. The

telescopes are mounted side-by-side on a Paramount MEII equatorial robotic mount driven by Software Bisque TheSkyX control software.

Recently, our SDA work has mainly been tied to the Phantom Echoes experiment [3,4], a collaborative effort between Australia, Canada, New Zealand, the United Kingdom and the United States, focused on rendezvous and proximity operations in GEO, using the two commercial dockings of the Mission Extension Vehicle-1 and 2 (MEV-1, MEV-2), operated by Northrop Grumman. The first docking, between MEV-1 and Intelsat 901, was successfully completed in February 2020, while the second one, between MEV-2 and Intelsat 10-02, took place in April 2021. The docking of MEV-1 was observed from New Zealand [2], as it took place over the Pacific Ocean. A number of photometric light curves of both MEV-1 and Intelsat 901 were collected, but only the data from Intelsat 901 were analysed for this paper. The observations and data reduction were already presented at the last year's AMOS conference [2], and will not be repeated here.

Recently, a new three-dimensional photometric model was developed at DTA to study the reflection of light from a satellite in GEO. This has enabled us to make predictions of the apparent visual magnitude of a satellite at any given time, based on the viewing and lighting geometries and on some assumptions about the properties of the materials used for the reflective surfaces. The aim of this work, however, was not to achieve a perfect match between the observations and the theoretical model, but rather to identify the key model elements, in order to explain the major features in the observed light curves.

2. THE PHOTOMETRIC MODEL

2.1 Satellite model

The satellite's body was modelled in three-dimensional space as a collection of flat facets. In this paper, the model of Intelsat 901 is presented. There are three major components to the model (Fig. 1): the satellite bus, two antenna reflectors and two solar panels along the vertical axis. The bus dimensions are $2.8 \text{ m} \times 3.5 \text{ m} \times 5.6 \text{ m}$, while the total span of the solar arrays is 31 m [5]. In normal operation, the solar bus always points to the earth (nadir). The solar panel axis stays perpendicular to the orbit (equatorial plane), while the front surface points towards the Sun (or rather to the same hour angle, as the Sun can be below or above the equatorial plane depending on the time of the year). The two antenna reflectors are turned towards the bus by a small angle. The exact amount of this rotation can be determined by examining the photometric light curve, as will be explained later in this paper.

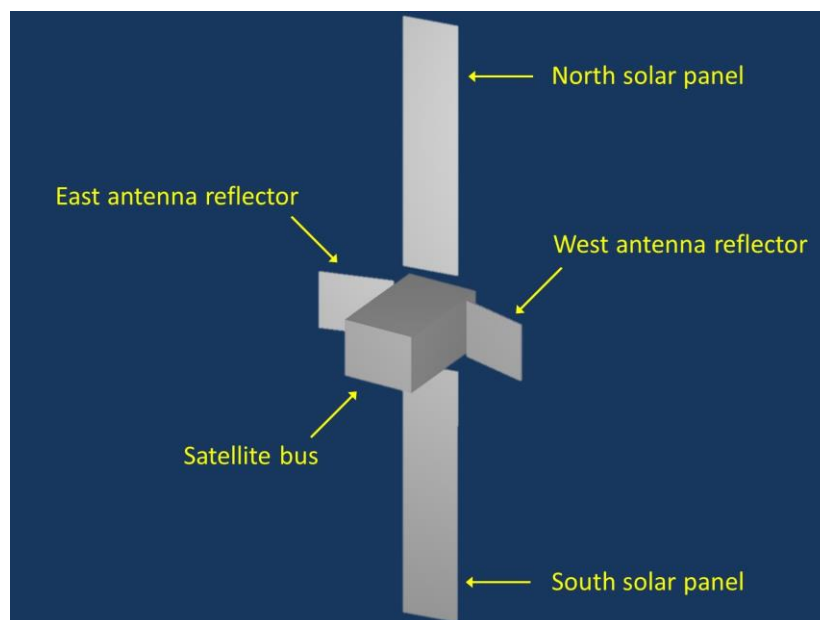


Fig. 1. A 3-D model of Intelsat 901.

2.2 Reflection of light

Each facet of the satellite model can be characterized by a set of reflectivity coefficients depending on the complexity of the model. In its simplest form, one can assume only the diffuse (Lambertian) reflection. While such model can be very useful for understanding the relative contributions of various sources of illumination (in particular the sunlight and earthshine components [6]), it was found that the diffuse reflection alone cannot fully explain the observational data. Our photometric model includes both the diffuse and specular components, and is based on the Ashikhmin-Shirley [7] bidirectional reflectance distribution function (BRDF), which is commonly used in physically-based computer rendering, but has also been utilized by a number of authors studying the photometric signatures of space objects [8]. The basic geometry of light reflection is shown in Fig. 2. A flat surface A with a normal vector \vec{n} is illuminated by a light source (Sun) from the direction \vec{k}_1 . The light is reflected towards the observer in the direction \vec{k}_2 . The bisector between \vec{k}_1 and \vec{k}_2 is given by the vector \vec{h} . All vectors are unit vectors, with \vec{k}_1 , \vec{k}_2 and \vec{h} belonging to the same plane (shaded grey in Fig. 2). The bisector \vec{h} forms the same angle with both \vec{k}_1 and \vec{k}_2 . The surface normal does not necessarily share the same plane with the other three vectors.

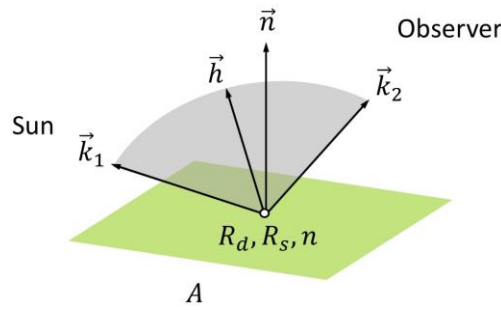


Fig. 2. Geometry of reflection

The reflective properties of the surface are described using a set of three parameters (R_d, R_s, n) representing the diffuse reflectivity, specular reflectivity and the Phong exponent, respectively (the Phong exponent n is not to be confused with the surface normal vector \vec{n}). The two reflectivity coefficients R_d and R_s must satisfy the energy conservation relation $R_d + R_s \leq 1$. Also, we have simplified the original Ashikhmin-Shirley anisotropic model by keeping only one Phong exponent, instead of two, i.e. assuming an isotropic case. If we denote the incident irradiance as dE_i and the reflected radiance as dL_r , then the BRDF is defined as:

$$\rho = \frac{dL_r}{dE_i}.$$

According to the Ashikhmin-Shirley model, this can be expressed as a sum of the diffuse and specular components:

$$\rho = \rho_{\text{diff}} + \rho_{\text{spec}},$$

which can be calculated using the following expressions:

$$\rho_{\text{diff}} = \frac{28R_d}{23\pi} (1 - R_s)(1 - \alpha^5)(1 - \beta^5),$$

$$\rho_{\text{spec}} = \frac{n + 1}{8\pi} \frac{(\vec{n} \cdot \vec{h})^n}{(\vec{h} \cdot \vec{k}) \max(\vec{n} \cdot \vec{k}_1, \vec{n} \cdot \vec{k}_2)} F,$$

where:

$$\alpha = 1 - \frac{\vec{n} \cdot \vec{k}_1}{2}, \quad \beta = 1 - \frac{\vec{n} \cdot \vec{k}_2}{2},$$

and the Fresnel term is:

$$F = R_s + (1 - R_s)(1 - \vec{h} \cdot \vec{k})^5.$$

In these equations, the scalar product $\vec{h} \cdot \vec{k}$ represents either $\vec{h} \cdot \vec{k}_1$, or $\vec{h} \cdot \vec{k}_2$, as they are identical. Once the BRDF is computed, the reflected flux becomes:

$$\Phi_A = \frac{\rho A (\vec{n} \cdot \vec{k}_1) (\vec{n} \cdot \vec{k}_2)}{d^2},$$

where A is the surface area, and d is the distance to the observer. This flux is relative to the solar flux received by the observer. The total flux reflected from a satellite made up of multiple facets is:

$$\Phi = \sum_i \Phi_i,$$

where the summation is over all facets illuminated by the Sun ($\vec{n} \cdot \vec{k}_1 > 0$), and at the same time visible by the observer ($\vec{n} \cdot \vec{k}_2 > 0$). Finally, the apparent magnitude is obtained as:

$$m = m_0 - 2.5 \log_{10} \Phi,$$

where $m_0 = -26.74$ is the apparent magnitude of the Sun at Earth's distance.

2.3 Occlusion and shadowing

Depending on the complexity of the satellite shape and the viewing and lighting geometries, we might have a situation where some parts of the body cast a shadow, preventing other facets from receiving the sunlight. At the same time, some facets might be occluded by other parts of the satellite when the model is viewed from the direction of the observer. This means that, even if the two scalar products ($\vec{n} \cdot \vec{k}_1$) and ($\vec{n} \cdot \vec{k}_2$) are both positive, i.e. when a facet is facing in the right direction to be both illuminated by the Sun and seen by the observer, the facet might still not contribute to the total flux. As an example, if we look again at the 3-D model in Fig. 1, we see that in this particular projection the satellite bus and the north solar panel are in clear view, however the east antenna reflector and the south solar panel are partially covered by the bus. We will see in the next section that the observer on Earth will practically always have a clear view of the entire satellite, and there will be no need for the occlusion analysis from that direction. However, the satellite bus will cast a shadow on one of the side antennas most of the time, depending on the lighting geometry. Our photometric model automatically finds the facets that are shadowed, and does not include them in the total flux calculation.

2.4 Earthshine

The DTA photometric model includes the earthshine component as an additional light source. This is the light reflected from the visible surface of the Earth towards the satellite. The total flux of the earthshine received by the satellite depends on the phase of the Earth, i.e. the fraction of the surface that is illuminated by the Sun. The earthshine can vary from zero, when the Sun is directly behind the Earth, to the fully illuminated globe when the Sun is directly behind the satellite. However, the earthshine is typically several orders of magnitude fainter than the sunlight and becomes noticeable only at large phase angles, beyond about 120° [6]. Modelling the earthshine is considerably more difficult than the direct sunlight. The Earth from space at the geostationary elevation of about 36000 km appears as an extended light source measuring about 17° , and cannot be modelled as a point source. As an additional difficulty, the surface brightness varies considerably across the disk and over time, depending on the seasonal changes and local cloud cover. The DTA photometric model integrates the reflected flux over the visible surface based on a season-dependent albedo map obtained from the Global Ozone Monitoring Experiment (GOME), an instrument aboard the European Space Agency's (ESA) Second European Remote Sensing Satellite (ERS-2) [9]. As an example, the albedo map for the month of February is shown in Fig. 3. Each pixel measures 1° in longitude and latitude. The pixel values are displayed as shades of grey between 0 (black) and 1 (white).



Fig. 3. Earth albedo map for the month of February based on the GOME-1 data

2.5 Moonlight

In certain situations, depending on the lighting geometry, the Moon can generate noticeable specular reflection from a space object. However, the moonlight is generally ignored, as it is typically by many orders of magnitude fainter than the direct sunlight. Only at large phase angles, when the contribution from the Sun becomes very low, the specular reflections from the Moon can be detected in the light curve. We did not have an opportunity to demonstrate this in our observations, but our model, in general, strongly suggested this possibility.

2.6 Geometric calculations

The DTA photometric model includes all necessary modules for viewing and lighting geometry calculations, based on the Jet Propulsion Laboratory's (JPL) solar system dynamics ephemeris DE441. This means that the positions of the Earth, Sun and Moon can be calculated for any given moment in time to match the observation data. Also, a built-in standard Simplified General Perturbations model SGP4 is used to propagate the satellite orbital position to the date of observation, based on a given set of Two-Line Elements (TLE). The apparent directions in space between the observer, satellite and light source are then adjusted for the light-time and rotated to the same reference frame using the International Astronomical Union's (IAU) Standards of Fundamental Astronomy (SOFA) library, in combination with the current values for the Earth orientation parameters (EOP). In this way, the model takes as an input only the satellite's TLE and the UTC date and time of observation, and generates the predicted apparent magnitude on output.

3. RESULTS

In order to demonstrate the photometric model described above, a single light curve of Intelsat 901 was selected from the MEV-1 data collection campaign, as shown in Fig. 4. The measurements were made on the night of 5th February 2020, between 10:00 and 16:00 UTC (22:00 – 04:00 New Zealand daylight savings time). The time scale is plotted on the bottom axis, while the corresponding solar phase angle (projected to the equatorial plane) is shown at the top. The phase angle is defined as the angle between the Sun and the observer, as seen from the satellite. Note that the phase angle of 0° (corresponding to the moment when the observer was between the Sun and the satellite) is off the chart to the left, as it occurred just before the start of observation. There were a few gaps in the data caused by the cloud cover, but they did not affect the modelling process. The light curve has a typical shape for a geostationary satellite, with a strong central peak generated by the specular reflection from the solar arrays, as the sunlight from the polished surfaces of the solar panels is reflected back towards the observer.

A preliminary analysis of the light curve revealed the following four interesting features:

1. A short period of practically constant brightness at about magnitude 11 was observed between 10:00 and 10:20 UTC, at the start of the observation night.
2. The brief initial plateau was then followed by a relatively steep rising slope, reaching a maximum of about 10.5 just before 11:00 UTC. Unfortunately, the satellite was in the cloud during the peak brightness.

However, the sky cleared soon after that, to reveal the falling slope of the light curve. There was no sign of any plateauing on that side of the central peak, as the brightness continued to drop steadily. It should also be noted that the maximum brightness was not recorded at zero phase, as otherwise would be the case if the solar arrays were perfectly aligned with the Sun. Instead, the magnitude peak occurred at about 16° , which means that the solar panels had an easterly offset of about 8° , i.e. lagging behind the Sun. The presence of such small offset in the orientation of the solar arrays is not uncommon, and was reported previously [10].

3. The third interesting feature was noticed between 12:00 and 12:30, at a phase angle of about 35° , when we detected a considerable brightening of the satellite, showing as a small bump on the falling slope of the light curve. The satellite was in the cloud when the event started, but when the sky cleared the light curve was raised by about a quarter of a magnitude above the earlier trend. Events like this usually happen when any additional facets on the satellite body are aligned in such a way to produce strong specular reflection. We will show later that this was caused by one of the two side antenna reflectors attached the satellite bus.
4. Finally, at around 14:30 (close to a phase angle of 65°) the light curve exhibited another prominent change in the brightness level and continued elevated by about half a magnitude above the earlier trend until the end of observation. At this stage, due to the relatively large phase angle, there were no additional facets that could generate such a change in the total brightness. Instead, our model suggested that the effect was caused by a small adjustment in the solar array offset angle.

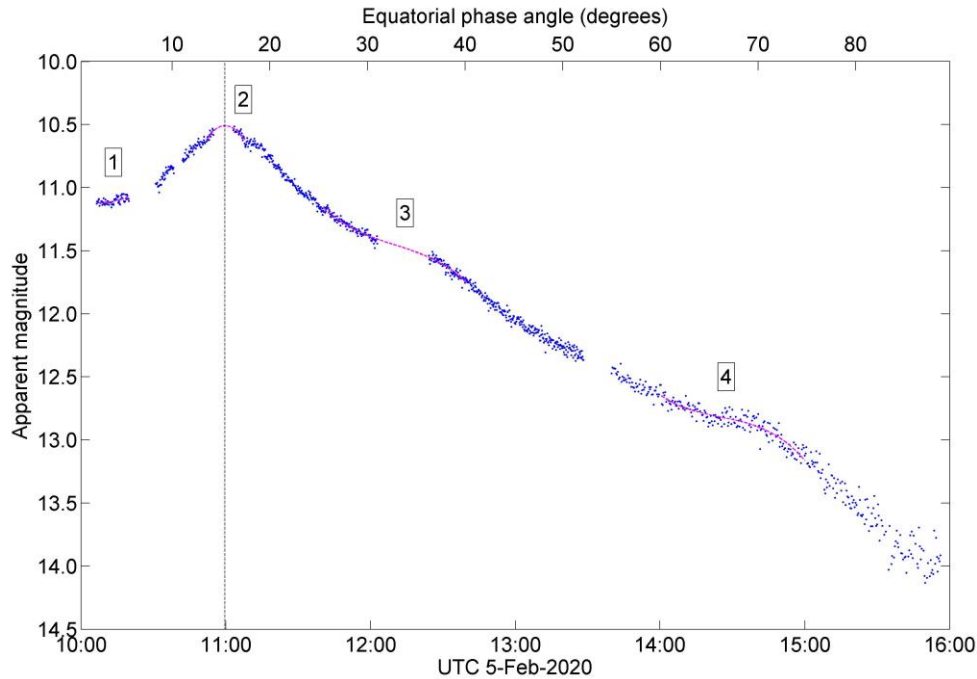


Fig. 4. The observed light curve of Intelsat 901 with some characteristic features labelled as described in the text.

In order to better understand some of the characteristic features of the observed light curve, a set of projected views of the satellite and the Earth were generated at every hour UTC on the 5th February 2020 between 10:00 and 16:00, as shown in Fig. 5. The top row represents the view from the observer, while the middle row presents the view from the Sun. In both projections the north is up, and the east is to the left. The bottom row shows the Earth, as seen from the satellite. Note that, at this time of the year, i.e. with the Sun still in the southern hemisphere, parts of Antarctica and the Southern Ocean are always illuminated, so the earthshine component will always be present in the photometric model, although it will be fainter by several orders of magnitude compared to the direct sunlight. Due to the fact that Intelsat 901 was close to the equatorial plane and to the east of the observing location, while the observer was located in the southern hemisphere, the satellite was seen slightly from the south and from the west. This view did not change significantly during the night. At the same time, the solar panels kept tracking the Sun, and were seen face-on at the start of observation, and close to edge-on towards the end. This change in the aspect angle of the solar arrays defined the overall shape of the light curve, reaching the maximum close to the time when the panels were seen face-on. It is also apparent from Fig. 5 that there was no significant occlusion to consider in the

photometric model, as all parts of the satellite were mainly in clear view. Note that the west antenna reflector reached a maximum brightness between 12:00 and 13:00, due to the small offset from the direction of the main bus axis. This resulted in an apparent brightening of the satellite which was detected in the light curve.

The view of the satellite from the Sun (middle row) shows a much more prominent change in the geometry. Apart from the very start of observation, at very low phase angles, when the view from the Sun was practically identical to the view from the observer, the satellite was mainly illuminated from the east throughout the night, causing the bus to cast a shadow on the west antenna reflector. The shadowing started to become more prominent just when the west antenna reached the maximum brightness after 12:00 UTC. This effect was included in our photometric model. However, note that the actual shadows are not shown in the observer views in Fig. 5, as the projections were generated using the standard OpenGL rendering for the simplicity of computation.

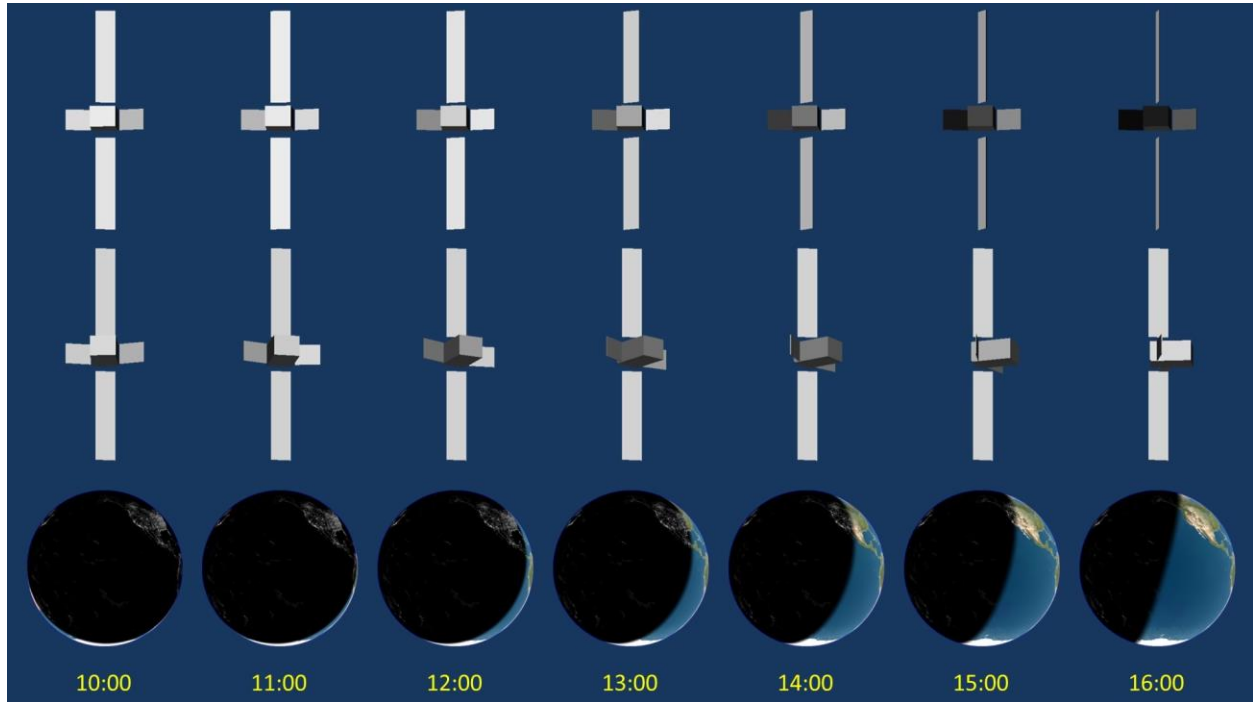


Fig. 5. Projected views of Intelsat 901 and Earth at specified UTC times on 5th February 2020.

The final results of the photometric model of Intelsat 901 are shown in Fig. 6, where the solid red line represents the best fit to the observation data. The modelling was performed in several stages:

1. As an initial step, the offset angle of the solar arrays was determined from the location of the light curve maximum. This was done by selecting only the solar panels in our 3-D model of Intelsat 901, and turning off the satellite bus and antenna reflectors. A satisfactory fit was obtained to the central peak between 10:30 and 11:30 UTC (phase angles between 8° and 23°). This gave a small eastward offset for the solar arrays with respect to the direction to the Sun of 8.2°. This offset was subsequently applied to the entire model throughout the night.
2. In a similar way, the tilt angle of the antenna reflectors with respect to the main axis of the satellite bus was determined by selecting only the antenna reflectors in the 3-D model and turning off the bus and solar arrays. The tilt was gradually adjusted until the peak brightness of the panels was placed at around 12:15, to match the apparent brightening of the satellite at that time, as recorded in the light curve. This gave a tilt of 15°, which was then fixed throughout the night. It was noticed during this process that the east antenna actually did not contribute much to the total brightness, due to its unfavourable orientation. However, the west antenna was positioned well to generate enough specular reflection for the brightening to be observed.
3. This was the main stage of the fitting process, where the entire satellite was used to match what we marked as the core observations between about 10:30 and 14:30, i.e. excluding the data from the very start and very

end of the night, when the observations appeared to be affected by a possible change in the attitude of the solar arrays. At this stage we had a total of nine free parameters to consider: the three reflection parameters (R_d, R_s, n) for the satellite bus, three more for the side reflectors (assuming that both reflectors were made of similar materials) and three parameters for the solar arrays. The parameter space was searched over a fixed grid by minimising the sum of the squares of the residuals between the predicted and observed apparent magnitudes. However, in order to speed up the computation process, some assumptions were made to reduce the number of the parameters. Firstly, it was found that the diffuse reflectivity of all parts of the satellite must stay below 0.1 in order to match the overall observed brightness. Initially, this was kept constant at 0.02 for all satellite components, but the value was slightly modified in subsequent runs in order to improve the overall fit. Also, it was noticed that the satellite bus contributed very little to the total brightness after the peak maximum, so it was decided to keep both the diffuse and specular reflectivity parameters of the bus fixed at some convenient values. As a result, only the specular parameters of the antenna reflectors and the solar arrays (four parameters in total) were varied. The result of this process is plotted as the solid green line in Fig. 6. The model showed a satisfactory fit to the data everywhere except for the central peak, where the model did not quite follow the steep rise of the data close to the maximum. One possible explanation for this mismatch is that the polar axis of the solar arrays might have had a small tilt towards the Sun. This would be enough to bring the surface normal closer to the Sun-observer bisector, which would in turn generate a sharper light curve peak. However, this possibility was not investigated further in this paper.

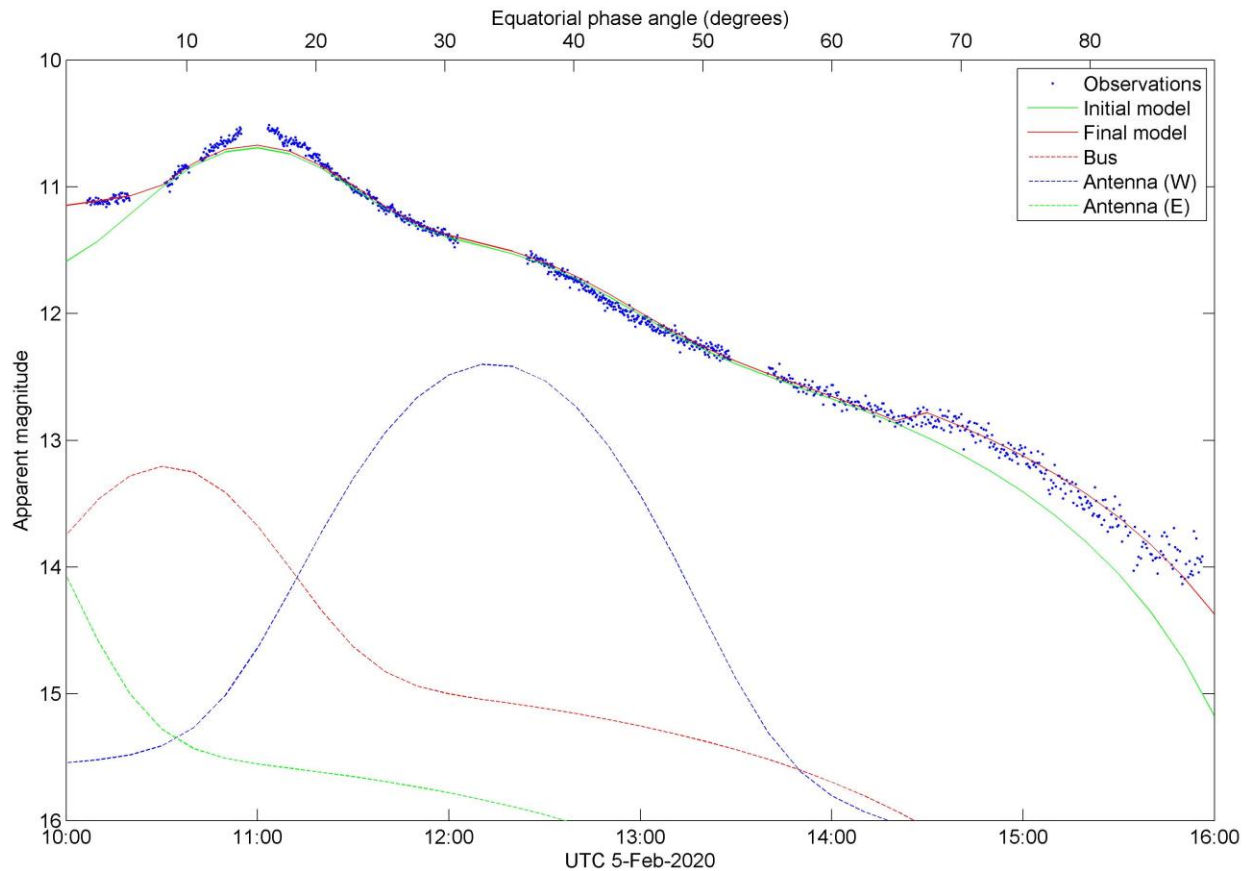


Fig. 6. The photometric model

4. As a next stage in the modelling procedure, the slightly raised tail of the light curve at the end of the night (after 14:30) was modelled by applying the core fit described above and then slowly varying the offset of the solar arrays. The best fit was obtained when the offset was changed from its nominal value of 8.2° to 13.5° , i.e. by about 5° .

5. Finally, the short plateau in the satellite brightness at the start of the night between 10:00 and 10:30 was modelled by introducing a gradual change in the solar array offset from 5.5° to 8.2°, i.e. by about 3° over 30 minutes.
6. The final light curve is shown as a solid red line in Fig. 6. It was calculated by adding the attitude changes of the solar arrays to the core model.

In addition to the overall photometric model (solid red and green lines), Fig. 6 also shows, for comparison, the individual photometric signatures of the satellite bus (dashed red line), east antenna reflector (dashed green line) and west antenna reflector (dashed blue line).

The final parameters of the model are listed below:

- Satellite bus: $R_d = 0.02$, $R_s = 0.5$, $n = 300$
- Antenna reflectors: $R_d = 0.01$, $R_s = 0.4$, $n = 200$
- Solar arrays: $R_d = 0.026$, $R_s = 0.3$, $n = 250$

where the tilt of the antenna reflectors was fixed at 15° towards the bus main axis, and the offset angle of the solar array was 8.2° to the east from the Sun most of the time during the night. No further analysis was made of the reflectivity parameters in terms of the physical properties of the materials, as the aim of this study was to obtain a satisfactory fit to the observations, so that the configuration of the satellite components could be studied.

4. SUMMARY

A three-dimensional physically-based light reflection model based on the Ashikhmin-Shirley anisotropic bidirectional reflectance distribution function was developed at the Defence Technology Agency (DTA) for monitoring the photometric signatures of space objects passing over New Zealand. In this model, a satellite is represented as a three-dimensional body in space composed of multiple facets, where each facet has its own light reflection properties. The model includes the direct sunlight, as well as the earthshine and moonlight as possible sources of illumination. The earthshine is computed by integrating the total surface albedo in visible light over the illuminated surface of the Earth, using the season-dependent albedo maps obtained from the GOME-1 data base. On input, the model takes the satellite's TLE and the time of observation, and on output it generates the apparent magnitude for the given geometry.

As an example, a light curve of Intelsat 901 was analysed during the docking operation of the Mission Extension Vehicle 1 (MEV-1) over the Pacific in February 2020. All observations were made from the DTA observatory at Whangaparaoa, near Auckland, New Zealand, using a 28-cm telescope and a full-frame CCD camera covering a field of view of about one degree diagonal. A total of six hours of observation were collected, covering the phase angles roughly between zero and 90°. The data revealed a number of interesting features in the light curve related to the orientation of various parts of the satellite.

It was demonstrated that inexpensive small-aperture equipment can successfully be used for photometric measurements of satellites in GEO, while the new three-dimensional photometric model was able to generate a satisfactory fit to the observation data, by varying the reflectivity properties of individual facets. This has enabled us to detect some small changes in the satellite's configuration, such as the offset angle of the solar arrays and the tilt of the antenna reflectors. This new ability will help in the further advancement of the New Zealand Defence Force space domain awareness capability.

5. REFERENCES

- [1] J. Skuljan. Photometric measurements of geostationary satellites over the Western Pacific Region, *Proc. 19th AMOS Conf.*, pp. 1420-1428, 2018
- [2] J. Skuljan. Astrometric and photometric measurements of GEO satellites in proximity operations over the Pacific, *Proc 21st AMOS Conf.*, 1374-1383, 2020
- [3] S. George, A. Ash, T. Bessell, L. Scott, J. Skuljan, J. Frith, R. Furfaro, V. Reddy. Phantom Echoes: A Five-Eyes SDA Experiment to Examine GEO Rendezvous and Proximity, *Proc 21st AMOS Conf.*, 97-114, 2020

- [4] S. George, A. Agathangelou, G. Privett, P. Halpin, W. Feline, A. Ash, L. Scott, J. Skuljan, J. Frith, J. Alvino, P. Chote. Phantom Echoes 2: A Five-Eyes SDA Experiment on GEO Proximity Operations, *Proc 22nd AMOS Conf.*, 2021
- [5] Arianespace Flight 141, 18th launch for Intelsat, https://www.arianespace.com/wp-content/uploads/2017/06/01_june_9-en.pdf
- [6] R. Cognion. Observations and modeling of GEO satellites at large phase angles, *AMOS Conf.*, 2013
- [7] M. Ashikhmin, P. Shirley. An anisotropic Phong light reflection model, *University of Utah Technical Report*, UUCS-00-014, 2000
- [8] R. Furfaro, R. Linares, V. Reddy. Shape identification of space objects via light curve inversion using deep learning, Pacific, *Proc 20th AMOS Conf.*, 161-177, 2019
- [9] J. P. Burrows, M. Weber, M. Buchwitz, V. Rozanov, et al. The Global Ozone Monitoring Experiment (GOME): Mission concept and first scientific results, *Journal of the Atmospheric Sciences*, Vol. 56, Issue 2, pp. 151–175, 1999
- [10] T. E. Payne, S. A. Gregory, K. Luu. SSA Analysis of GEOS photometric signature classifications and solar panel offsets, *AMOS Conf.*, 2006